ADVANCED MATERIALS
www.advmat.de

Modulating Trapping in Low-Dimensional Lead–Tin Halides for Energy-Efficient Neuromorphic Electronics

*Lijun Chen, Saad Saleh, Filippo Tavormina, Lorenzo Di Mario, Jiaxiong Li, Zhiqiang Xie, Norberto Masciocchi, Christoph J. Brabec, Boris Koldehofe, and Maria Antonietta Loi**

Metal halide perovskites have drawn great attention for neuromorphic electronic devices in recent years, however, the toxicity of lead as well as the variability and energy consumption of operational devices still pose great challenges for further consideration of this material in neuromorphic computing applications. Here, a 2D Ruddlesden-Popper (RP) metal halides system of formulation $BA_2Pb_{0.5}Sn_{0.5}I_4$ (BA = *n*-butylammonium) is prepared that exhibits outstanding resistive switching memory performance after cesium carbonate (Cs_2CO_3) deposition. In particular, the device exhibits excellent switching characteristics (endurance of 5×10^5 cycles, ON/OFF ratio $\approx 10^5$) and achieves 90.1% accuracy on the MNIST dataset. More importantly, a novel energy-efficient content addressable memory (CAM) architecture building on perovskite memristive devices for neuromorphic applications, called nCAM, is proposed, which has a minimum energy consumption of ≈0.025 f) bit/cell. A mechanism involving the manipulation of trapping states through Cs_2CO_3 deposition is proposed to explain the resistive switching behavior of the memristive device.

1. Introduction

Neuromorphic computing based on resistive switching devices is a brain-inspired technology that is emerging as a potential alternative to CMOS electronics for implementing power- and size-efficient artificial intelligence applications.[1] Neural network computing algorithms implemented with traditional hardware platforms face a few drawbacks, such as excessive latency, energy consumption, and scalability.[2] In these cases, training a neural network takes a large amount of time and computational resources, which is not comparable to biological brain learning with little supervision. It is worth mentioning that two-terminal memristors have been proven to be capable of emulating neuronal and synaptic functions, and memristor-based neural network computing benefits from their physical resemblance of local activity as well as dense interconnectivity to the brain.[3] Therefore, developing reliable and efficient memristors with a wide range of memory characteristics and specialized memory architecture has become a highly promising path toward improving neuromorphic computing.

Metal halide perovskite memristors have attracted considerable attention after the resistive switching behavior was observed in $MAPbI_3$ (MA = methylammonium) ≈10 years ago.[4,5] Their promising memristive properties show that metal halide perovskites have great potential for information storage and computation.[6,7] In addition, perovskite devices could also benefit from their easy manufacturing, fast switching speed,[8] mechanical flexibility,[9] and low energy consumption.[10] Lead halide perovskites have demonstrated

L. Chen, F. Tavormina, L. Di Mario, J. Li, C. J. Brabec, M. A. Loi
Zernike Institute for Advanced Materials
University of Groningen
Nijenborgh 4, Groningen 9747 AG, The Netherlands
E-mail: m.a.loi@rug.nl

S. Saleh
Bernoulli Institute
University of Groningen
Nijenborgh 9, Groningen 9747 AG, The Netherlands

The ORCID identification number(s) for the author(s) of this article can be found under https://doi.org/10.1002/adma.202414430

DOI: 10.1002/adma.202414430

L. Chen, S. Saleh, B. Koldehofe, M. A. Loi
CogniGron (Groningen Cognitive Systems and Materials Center)
University of Groningen
Nijenborgh 4, Groningen 9747 AG, The Netherlands

F. Tavormina, N. Masciocchi
Dipartimento di Scienza e Alta Tecnologia and To.Sca.Lab
Università dell'Insubria
via Valleggio 11, Como I-22100, Italy

Z. Xie, C. J. Brabec
Institute of Materials for Electronics and Energy Technology (i-MEET)
Department of Materials Science and Engineering
Friedrich-Alexander-University
Erlangen-Nürnberg Martensstrasse 7, 91058 Erlangen, Germany

B. Koldehofe
Department of Computer Science and Automation
Technische Universität Ilmenau
Helmholtzplatz. 5, 98693 Ilmenau, Germany

good operating performances for pattern recognition[11–16] physical unclonable functions,[17] logic operations,[18] and mechano-nociceptive systems,[19] etc. Unfortunately, after mapping the weight of the neural network to the conductance value of the memristor crossbar, the poor reproducibility of the device in switching, and the no-ideal erase/write characteristics deteriorate largely the accuracy of computations.[20,21] Therefore, to give metal halide perovskites a chance in neuromorphic computing, it is necessary to develop robust materials with high repeatability (low cycle-to-cycle and device-to-device variabilities). Furthermore, non-harmful compositions and scalable fabrication would be preferred when moving toward possible applications. To this goal, metal halide perovskite materials with limited toxicity (Sn-based,[22] Sn—Pb,[23] and others[24–28]) are investigated in-memory applications. However, these devices often demonstrate lower endurance and retention performance compared to pure lead-based devices.

It is also important to note that, for neuromorphic systems, there is a strong emphasis on the development of specialized memories that are different from regular static or dynamic random-access memories. Content addressable memory (CAM) has the capability of matching the incoming data against locally stored rules and taking corresponding actions. In neuromorphic systems, CAMs can mimic human memories based on the data received from sensory signals.[29] However, the state-of-the-art CAM architectures built heavily on binary computations face severe energy issues and storage limitations. Recently, an analog CAM design was proposed for more expressive storage operations by efficiently utilizing the highly tunable analog conductivity and multiple stable intermediate states in memristive devices.[30,31] Here, we demonstrate the potential of implementing this emerging analog CAM architecture using newly proposed perovskite memristive devices for energy-efficient neuromorphic computing.

We fabricated memristive devices with robust 2D layered RP metal-halide materials of composition $BA_2Pb_{0.5}Sn_{0.5}I_4$ deposited by blade coating, a drastic improvement of the memory properties was found after Cs_2CO_3 was deposited on the metal halide surface due to the controllable introduction of additional trap states, primarily driven by the formation of new low-dimensional phases. This Cs_2CO_3-based strategy has not been reported previously. As substantiated below, silver-top electrode devices exhibited nonvolatile properties but lacked reliability, whereas the gold-top electrode devices exhibited good volatile characteristics, including an endurance of 5×10^5 cycles (ranking among the best for lead-less/free halide perovskite memristive devices) and an ON/OFF ratio of $\approx 10^5$, and achieved MNIST pattern recognition with 90.1% accuracy. By temperature-dependent impedance and photoluminescence spectroscopy, we investigated the origin of the memristive properties, which is determined by the modulation of the trap state landscape. More importantly, we propose a novel RP perovskite memristor-based analog nCAM architecture for performing line-rate operations in neuromorphic computing systems. As a result, the proposed perovskite-based nCAM showed a minimum energy consumption of ≈ 0.025 fJ bit^{-1} per cell, making it one of the most energy-efficient devices reported to date.

2. Results and Discussion

Thin films of 2D RP phases with the composition $BA_2Pb_{0.5}Sn_{0.5}I_4$ were fabricated by blade-coating as depicted in **Figure 1a**. The detailed process is described in the experimental section of the Supporting Information. As seen from the scanning electron microscopy (SEM) and atomic force microscopy (AFM) images, 2D perovskite films exhibit large grain size (≈20 µm) and a rather homogenous surface with an RMS roughness of ≈60 nm (Figure 1b,d). To obtain desirable memory properties, we introduced a thin layer of Cs_2CO_3 on the perovskite surface to increase the number of charge-trapping states. Figure 1c,e demonstrates that small sub-micrometer particles appear on the surface of the sample upon deposition of Cs_2CO_3, resulting in a larger RMS roughness. The UV–vis absorption spectra (Figure S1a, Supporting Information) and X-ray diffraction (XRD) patterns (Figure S2, Supporting Information) show that after Cs_2CO_3 deposition both the absorbance and the structural properties of highly oriented perovskite films are maintained. The FTIR spectra of the film with Cs_2CO_3 deposition revealed stretching vibration peaks of the COO^- groups within the range of 1400–1500 cm^{-1} (Figure S1b, Supporting Information). Grazing-Incidence Wide-Angle Scattering (GIWAXS) measurements provide further evidence concerning the effect of Cs_2CO_3, which results in sample modifications involving both the intensity and breadth of the Bragg spots and the formation of different phases, as evidenced by the appearance of some extra reflections (see Figure 1f,g). The 2D layered RP $BA_2Pb_{0.5}Sn_{0.5}I_4$ film showed the presence of highly oriented 2D phases along the [001] crystallographic direction, with the (00*l*) planes parallel to the substrate surface (Figure S3, Supporting Information). After the Cs_2CO_3 deposition, the 2D RP phase exhibited a minor loss of orientational degree (texture), as demonstrated by the appearance of arcs around its Bragg spots, while two additional crystal phases appeared. These were recognized to be the quasi-2D mixed-cation $BA_2Cs(Pb_{0.5}Sn_{0.5})_2I_7$ phase (*Bbm*2) and the 0D Cs_2SnI_6 phase, as confirmed by the Bragg-spot indexing shown in Figure S4 (Supporting Information). These additional phases, featuring low dimensionality, may act as charge-storage elements. Carriers are injected from the electrodes and are stored in the trap states and subsequently extracted at higher voltages. The SEM-Circular Backscatter Detector (CBS) images showed the mapping of the spatial phase distribution of Pb—Sn perovskite with and without surface treatment (Figure S5, Supporting Information).

Memristive devices with ITO/PEDOT:PSS/$BA_2Pb_{0.5}Sn_{0.5}I_4$/(w/wo) Cs_2CO_3/Au structure (**Figure 2a**) were fabricated. The bottom contact incorporates a PEDOT:PSS layer, which effectively reduces the roughness of the ITO substrate and provides a smooth surface for the low-dimensional system to grow as a continuous layer. All samples exhibited volatile resistive switching behavior with a voltage sweeping cycle of $0 \rightarrow 2 \rightarrow 0 \rightarrow -2 \rightarrow 0$ V, even under current compliance (I_{cc}) of 10 µA, as illustrated in Figure 2b and Figure S6 (Supporting Information). Notably, a much higher on/off ratio $\approx 10^5$ is obtained after the deposition of Cs_2CO_3, due to the different resistance values of the high resistance state (HRS) and low resistance state (LRS). The devices also showed good *I*–*V* curve consistency after 40 successive cycles of scanning (Figure S7a, Supporting Information) or after storage in an inert atmosphere for 5 months (Figure S7b, Supporting

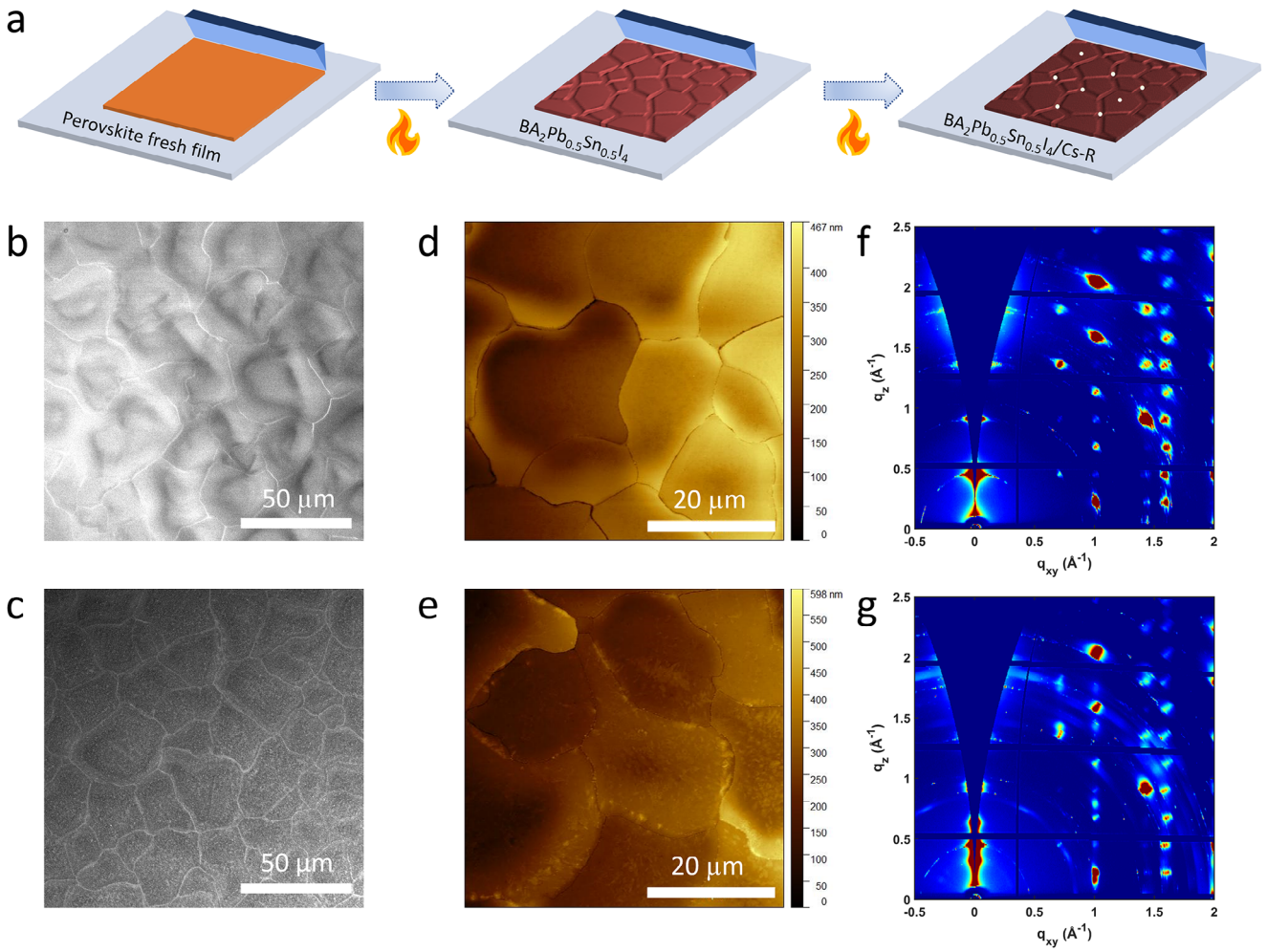

Figure 1. Perovskite films morphology and crystallization behavior. a) Schematic of preparation process of 2D Pb—Sn perovskite and surface treatment with blade coating. b) SEM, d) AFM, and f) GIWAXS measurements of perovskite films without Cs_2CO_3. c) SEM, e)AFM, and g) GIWAXS measurements of perovskite samples with Cs_2CO_3.

Information). The average set voltages obtained from either 40 cycles or 20 memory cells showed a narrow distribution (Figure S8, Supporting Information), ensuring good cycle-to-cycle and device-to-device reproducibility. On the other hand, a nonvolatile resistive switching behavior with a lower set voltage was observed when the top electrode was replaced with Ag (without I_{cc} or with I_{cc} of 10 μA, Figure 2c; Figure S6, Supporting Information), an effect which we attribute to Ag ionic movement and electrochemical reactions at the $BA_2Pb_{0.5}Sn_{0.5}I_4$/Ag contact interface (vide infra). Still, a similar trend with an enhancement of the on/off ratio (≈10^3) was observed with the deposition of Cs_2CO_3, but these devices suffered from cycling variability and storage instability (Figure S9, Supporting Information).

Therefore, we decided to focus on devices with Au electrodes for further investigation. In addition, cesium acetate (CH_3COOCs) and polymethyl methacrylate (PMMA) were also used on the metal halide layer to investigate the universality of our surface trap states regulation strategy. As shown in Figure S10 (Supporting Information), the treatment with CH_3COOCs also greatly improved the on/off ratio, while devices using PMMA showed a more limited current level at HRS, highlighting the importance of our optimization strategy based on the introduction of small amounts of Cs and the formation of $BA_2Cs(Pb_{0.5}Sn_{0.5})_2I_7$ (*Bbm*2) and the 0D Cs_2SnI_6 phases at the interface.

Encouraged by the low cycle-to-cycle and device-to-device variability of memristive devices with Cs_2CO_3 and Au electrodes, additional functionalities were investigated. As substantiated in Figure 2d, the optimized volatile device showed a highly robust endurance of over 5×10^5 cycles with write voltage (2 V,100 ms) and read voltage of 0.2 V. Such a high endurance stands out as one of the best among reported halide perovskites-based memristors characterized by being Pb-free or possessing a low Pb-content (see Table S1, Supporting Information). Furthermore, their long-term stability makes them highly promising for further real-life applications.

The spike-timing dependent plasticity (STDP) behavior of our devices was found to follow an asymmetric Hebbian rule (Figure 2e), where the synaptic weight variation (dW) depends on the relative arrival time of presynaptic and postsynaptic signals. When the presynaptic pulses (2 V/20 ms) are applied

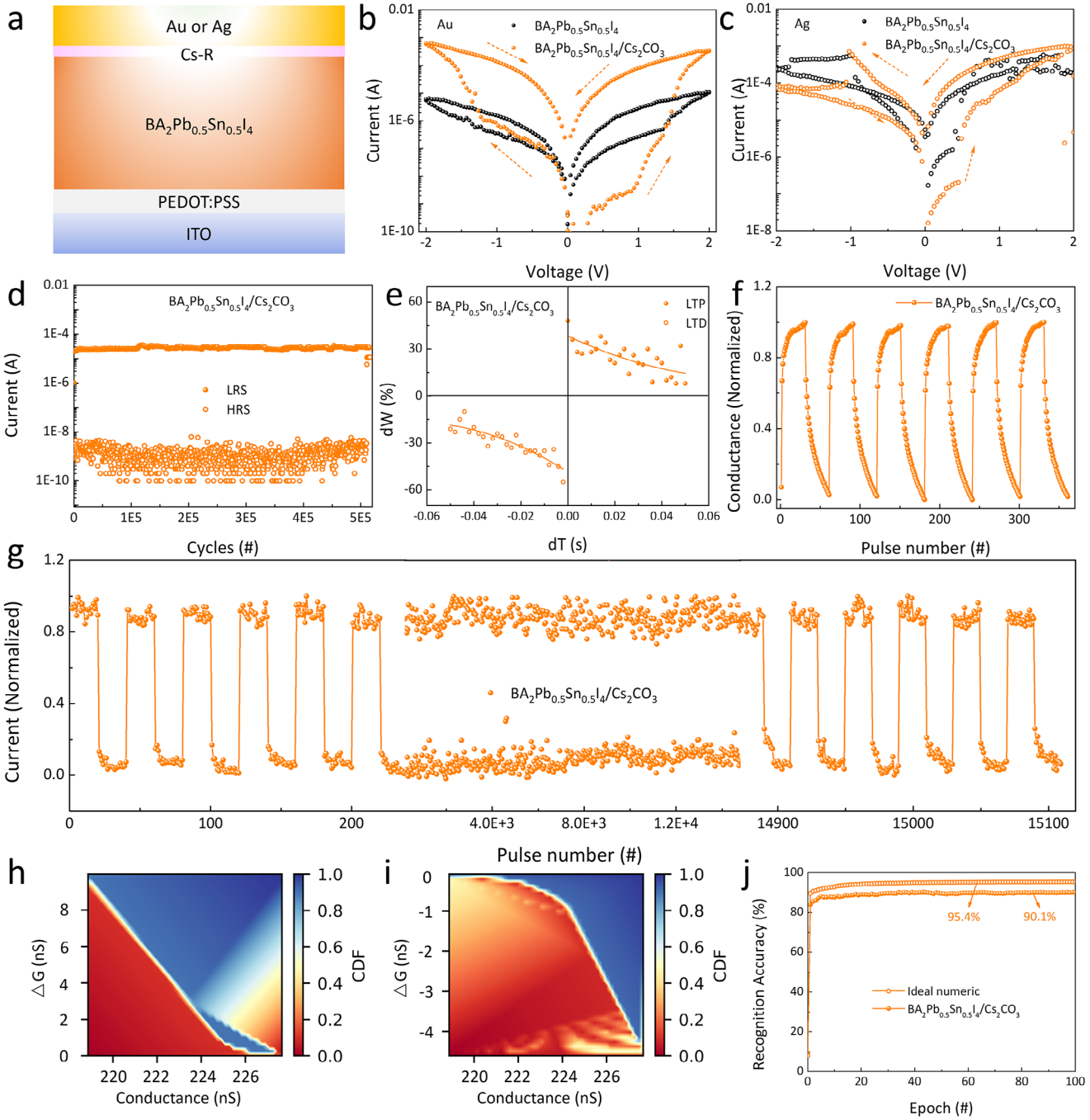

Figure 2. Memory performance and synaptic properties. a) Schematic of the perovskite-based memristor device structure. b) *I–V* characteristics of devices with Au electrodes and c) Ag electrodes, both measured without current compliance under dark conditions. d) Endurance performance. e) STDP behavior. f) Potentiation and depression characteristics of memristive device with Cs_2CO_3. g) Operational stability measurement of the optimized perovskite device with 15 100 pulse cycles. h,i) Heatmap representation of the ΔG versus G switching properties during (h) potentiation and (i) depression, the color represents the cumulative distribution function (CDF) at each conductance state. j) Accuracy evaluation of the proposed perovskite-based neural network for the MNIST dataset.

before the postsynaptic pulses (−2 V/20 ms), the synaptic weight is strengthened, otherwise the synaptic weight is weakened. It is noteworthy that activity within the millisecond time range is particularly interesting for interfacing neuromorphic devices with biological systems, as these response times are comparable to those of biological synapses. The retention time was further studied using time-resolved repeated pulse stimulation. As shown in Figure S11a (Supporting Information), the normalized conductance weight can retain 20% of the last stimulated state after applying a sequence of ten identical input pulses with an amplitude

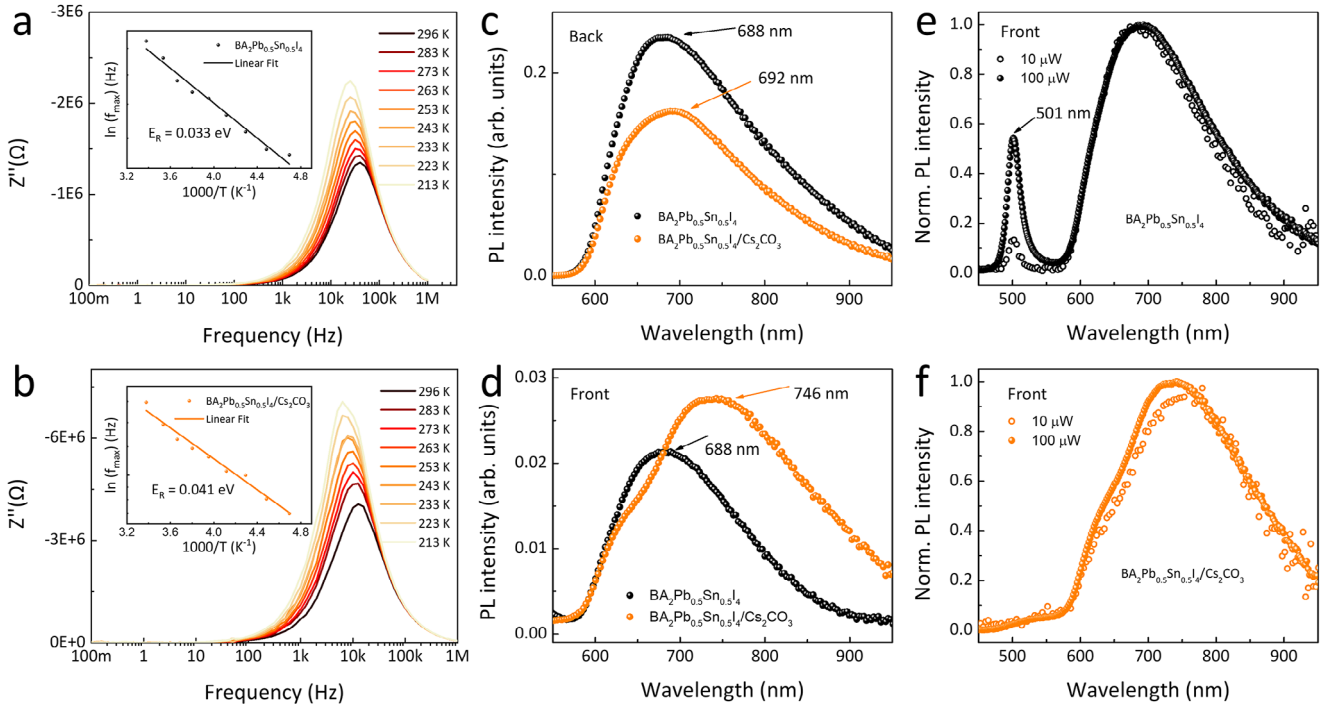

Figure 3. Conduction mechanisms of the perovskite artificial synapses. a,b) Imaginary Z″ part of the impedance as a function of frequency at different temperatures of memristor without (a) and with (b) Cs_2CO_3. c,d) Photoluminescence spectra of the two films excited from the back (c) and front (d) side. e,f) Photoluminescence spectra of $BA_2Pb_{0.5}Sn_{0.5}I_4$ (e) and (f) $BA_2Pb_{0.5}Sn_{0.5}I_4/Cs_2CO_3$ with different optical pump fluence.

of 2 V, a width of 1 ms, and an interval of 30 ms, indicating that our devices are short-term memories that can be refreshed after the device loses its state in the nCAM architecture.

While good switching characteristics are essential for simulating synapses, low-variability potentiation, and depression are also required for neuromorphic applications. The reference device (Au electrode) showed high-noise conductance transformation with 360 pulses (Figure S11b, Supporting Information, pulse height of 2 V, width of 100 ms, interval of 20 ms, and read voltage of 0.2 V), while high linearity and symmetry of the weight updates was observed for the same 360 pulse cycles using the Cs_2CO_3 modified device (Figure 2f). Moreover, the device sustained stable operation for more than 15 100 cycles under input with a longer pulse interval of 300 ms (Figure 2g), showing highly reproducible switching behavior without changes in the overall conductivity. Taking advantage of the highly consistent and linear conductance states, we simulated the function of a simple three-layer (one hidden layer) neural network based on backpropagation for identifying the MNIST (28 × 28-pixel version of handwritten digits) database, as depicted in Figure S12a (Supporting Information). The numerical weights in the network layer were mapped directly onto the experimentally measured conductance states of our devices. Figure S12b (Supporting Information) shows the circuit schematic of the crossbar array, which performs vector-matrix multiplication and parallel rank one outer product update. The heat maps of the conductance change (ΔG) and conductance (G) switching statistics of long-term potentiation and depotentiation are presented in Figure 2h,i. As a result of the highly reproducible and noiseless synaptic conductance states, our device with Cs_2CO_3 gave a recognition accuracy of 90.1% after neural network training (Figure 2j). For the memristive devices with Ag top electrode, as shown in Figure S13 (Supporting Information), the performance in terms of endurance (3×10^4 cycles) and potentiation and depression (240 pulses) is slightly poorer than for devices using Au, and the recognition accuracy reaches 82.4% with 50 training epochs (Figure S14, Supporting Information). It is important to emphasize that all our testing and device storage were conducted in a nitrogen atmosphere due to the sensitivity of Sn to environmental exposure.

To reveal the transport and switching mechanism behind the functioning of our memristive devices, temperature-dependent impedance spectroscopy (TDIS) measurements are presented in **Figures 3** and S15 (Supporting Information). Low-dimensional metal halides contain a series of trap states with distinct formation energy distributions,[32] and it has been proposed that charge trapping and de-trapping phenomena would influence space charge accumulation and electric field distortion, hence, their electrical resistive properties before and after the switching operation. In our TDIS measurements, we observed high-frequency (10^3–10^5 Hz) signals, see Figure 3a,b, which can be used to analyze the activation energy of trapping states and their density, within the active material or at the interfaces. The imaginary impedance (Z″) plotted against frequency at different temperatures shows two evident effects: i) the relaxation peaks shifting to lower frequency with decreasing temperature, and ii) the same peaks shifting at lower frequencies after Cs_2CO_3 deposition. The activation energy (E_R) involved in the relaxation process can be determined using the Equation (1):

$$f_m = f_0 \exp\left(-E_R/kT\right) \quad (1)$$

where f_m represents the peak frequency, f_0 is a pre-exponential factor, k is Boltzmann's constant, and T is the absolute temperature. The insert of Figure 3a,b shows the Arrhenius plot of $\ln(f_m)$ against 1000/T, the linear fitting yields E_R = 0.033 eV for $BA_2Pb_{0.5}Sn_{0.5}I_4$ and E_R = 0.041 eV for $BA_2Pb_{0.5}Sn_{0.5}I_4/Cs_2CO_3$, both values being consistent with earlier literature.[33] The enhanced activation energy of the relaxation process for the sample with Cs_2CO_3 suggests a higher trap density, which allows an improved contrast between the before and after trap-filling and thus an increase of the resistive switching performance. Figure S16 (Supporting Information) shows the Bode plot of both Au-based devices under various biases, where the reduced semicircle sizes with increasing bias are in line with the device transferring from the HRS to the LRS. However, there is no low-frequency capacitance signal, indicating minimal ion movement during device operation. Therefore, in Au-based devices, the operation is primarily attributed to the process of trap filling and gradual trap emptying. In contrast, for devices with Ag top electrodes, as shown in Figure S17 (Supporting Information), the appearance of negative capacitance is closely associated with a slow kinetic phenomenon involving Ag ionic migration and electrochemical reactions at the $BA_2Pb_{0.5}Sn_{0.5}I_4$/Ag contact interface.[34] In addition, their UV irradiated-dependent impedance spectra illustrate that the device can also be modulated by optical signals (Figure S18, Supporting Information), fostering great potential for artificial synapses.

Steady-state and time-resolved photoluminescence (PL) spectra were investigated to further assess the density of trap states in the active layer with or without Cs_2CO_3. Samples were measured exciting them from both sides, to verify the effects of the treatments on the entire thickness of the material. Figure 3c,d and Figure S19 (Supporting Information) demonstrate that the $BA_2Pb_{0.5}Sn_{0.5}I_4$ film showed an identical PL peak position (688 nm) and spectral shape when measured on the front and back sides, showing the same trapping density at the top and bottom surfaces of the devices. However, the PL peak on the back side of the perovskite film is red shifted to 692 nm after Cs_2CO_3 treatment, while the front side shows a more significant shift to 746 nm, along with a high-energy shoulder reminiscent of the pristine material. We interpret this completely different PL spectrum due to the presence of the previously mentioned $BA_2Cs(Pb_{0.5}Sn_{0.5})_2I_7$ and Cs_2SnI_6 phase acting as an energy transfer sink for the PL signal.

The spontaneous radiative recombination from trap states can lead to minor emission peak red-shifts from the values except for a band edge transition.[35] According to our observations, Cs_2CO_3 introduced additional perovskite phases and charge traps on the surface where it has been deposited. In addition, upon UV irradiation, the sample without Cs_2CO_3 shows a strong and narrow PL peak at 501 nm that increased in relative intensity with pump fluence, which is attributed to the photoinduced degradation or segregation of SnI_2 and PbI_2 as it was reported in our previous work.[36] The PL signal is expected to be dependent on pump fluence and time of exposure to the laser. As shown in Figure 3e and Figure S20 (Supporting Information), the peak intensity at 501 nm increases rapidly after laser exposure while the signal at 688 nm decreases. Differently, in the sample with the extra Cs_2CO_3 layer, such a signal is not found even after several minutes of laser exposure (Figure 3f). The inhibited phase segregation is extremely important for the reproducibility and reliability of the perovskite memristive properties, and is confirmed by the improved device endurance and cycling stability after Cs_2CO_3 deposition. Time-resolved photoluminescence of both films shows long dynamics from the back side and short dynamics from the front side (Figure S21, Supporting Information). The PL lifetimes of two samples exhibit slight differences when excited from the back side (≈225 ps with Cs_2CO_3 and 227 ps without Cs_2CO_3), while, in the front side, faster dynamics are observed for the Cs_2CO_3-treated sample than for untreated one (≈171 vs 200 ps, respectively) (see Table S2, Supporting Information). This is consistent with the increased trap density noted from the PL spectra. Overall, the results of impedance and optical spectroscopy coherently indicate that the modification of the density of trap states is the main source of resistive switching in our samples. In conclusion, the device characteristics reported in Figure 2b,c depend on the nature of the active layer, the presence of Cs_2CO_3, and the choice of electrodes.

Based on the developed memristive devices, we propose a novel nCAM architecture that stores the rules for neuromorphic systems in the form of programmed resistances of the perovskite-based memristive devices. The nCAM performs a search operation by matching the incoming data (sensory signals) against the locally stored rules (actual memories): if the incoming data matches the stored rules, the output is high; otherwise, the output drops.[37] The major components of our nCAM architecture include two perovskite memristive devices (m_0 and m_1), one resistor (R_x), and five transistors as shown in **Figure 4a**. The rule range [$V_{IN(A)}$, $V_{IN(B)}$] of nCAM is stored inside the cell by programming the resistances of two memristive devices into states M_0 and M_1, respectively. This occurs during the write operation when the write line (W) is enabled and the set voltage is applied through lines S_0 and S_1. During the search operation, input data V_{IN} and a set of read voltages V_{DD} (1 V) were applied where line C_0 is enabled. The developed voltages V_A and V_B, whose relationships with the memristive states (M_0 and M_1) are described in Equations (2) and (3), modulate transistors T_0 and T_1 to produce the result of the match operation. The use of memristors thus presents an exciting opportunity for facile and drastic modification of the matching range at the write stage, in an area- and energy-economic manner. More operation details can be found in Tables S3 and S4 (Supporting Information).

$$V_A = \frac{M_0}{M_1 + M_0 + R_X}\left(V_{DD} - V_{IN}\right) + V_{IN} \tag{2}$$

$$V_B = \frac{M_0 + M_1}{M_0 + M_1 + R_X}\left(V_{DD} - V_{IN}\right) + V_{IN} \tag{3}$$

Figure 4b presents the abstract operation of the proposed nCAM in neuromorphic systems. The analog voltage values are applied as inputs (such as t_1 = 0.8 (colors), t_2 = 0.2 (numbers), and t_3 = 0.3 (...)) to multiple parallel nCAM cells during the search operation, and each nCAM cell produces high or low match signal based on the resemblance of inputs with the stored rule, the latter encoded by multilevel resistances in the memristors (see Note S1, Supporting Information for details). The transistors can be analyzed based on their gating, as governed by Equations (2) and (3), to provide analog matching results that reflect the proximity of input data to the set boundaries. This allows for a

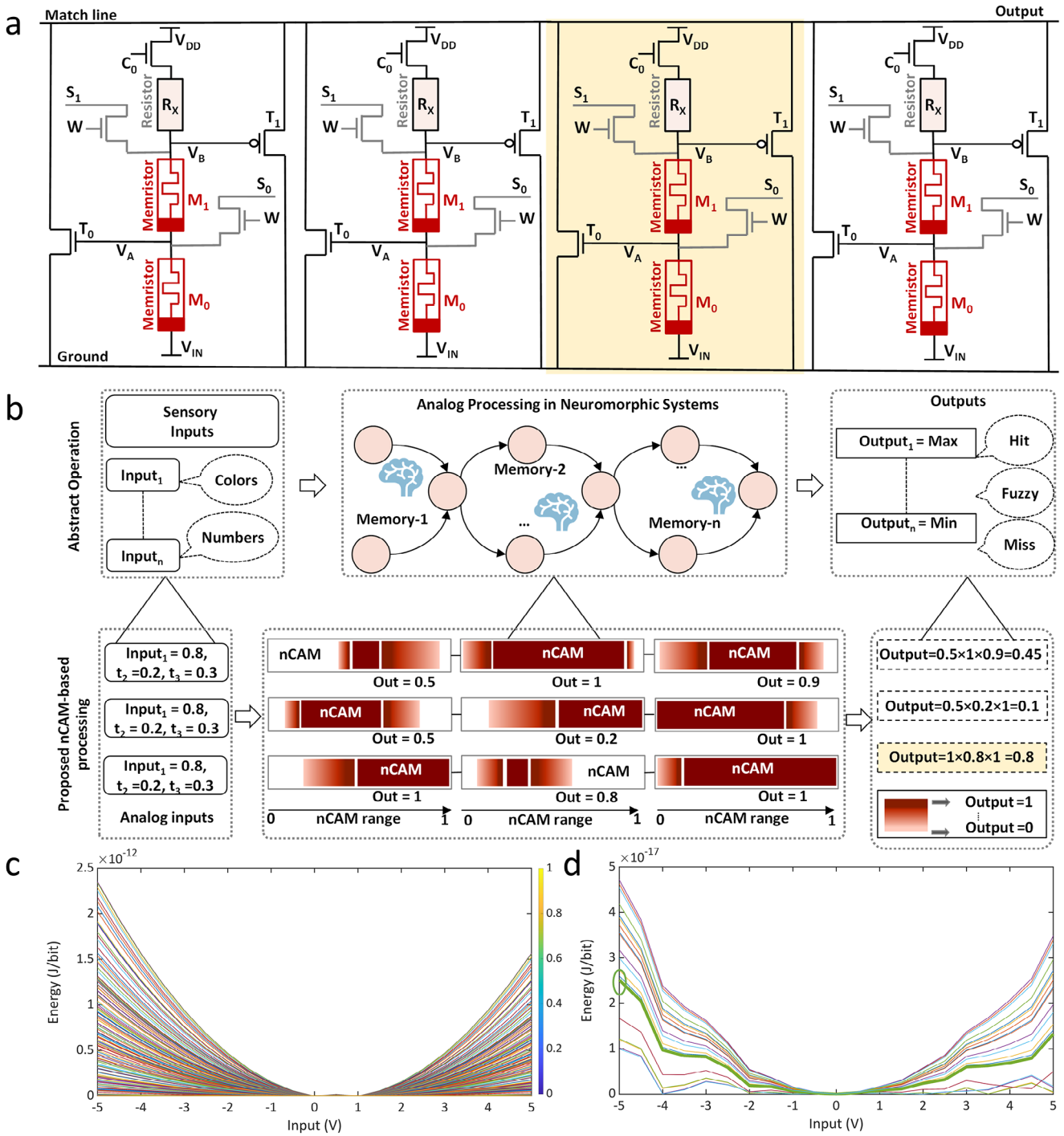

Figure 4. Neuromorphic computing with perovskite-based memristive devices. a) Schematic of the proposed circuits for nCAM, composed of five transistors, two memristors, and one resistor. b) The abstract operation of proposed nCAM-based processing for neuromorphic systems. c) Energy consumption of nCAM made from $BA_2Pb_{0.5}Sn_{0.5}I_4/Cs_2CO_3$ with Au electrode. d) The selected lowest energy consumption states from (c).

continuum between a clear hit and miss, representing the inherent fuzziness of the memory.[30] On the architectural level, multiple nCAM cells can be combined in series to achieve the product of several serial matches, enabling a multistage match-action process for higher-dimensional verification tasks. Figure 4b shows the outputs are 0.45, 0.1, and 0.8, respectively, based on three different programmed rules. Benefiting from the unique properties of perovskite memristors, we demonstrate the operation of the proposed memristor-based nCAM by assigning various resistance states to M_0 and M_1 and simulating their behavior under different input voltage levels. The output results based on the experimental dataset of perovskite-based memristive devices are

shown in Figure S22 (Supporting Information), which demonstrates that the nCAM, with its variable conductance combinations, maps analog inputs across a wide range, yielding a unique output for each input.

The performance of the proposed nCAM is further evaluated in terms of the energy consumption during the search operation. The experimental dataset of four memristive devices, i.e., Au-based and Ag-based $BA_2Pb_{0.5}Sn_{0.5}I_4$ and $BA_2Pb_{0.5}Sn_{0.5}I_4/Cs_2CO_3$, was used in the simulation model of the proposed nCAM. The energy consumption of the nCAM for Au-based $BA_2Pb_{0.5}Sn_{0.5}I_4/Cs_2CO_3$ and the other three devices are shown in Figure 4c and Figure S23 (Supporting Information), respectively. The variation of input voltage in the range [−5 V,+5 V] shows a nonlinear relationship to the energy consumed by nCAM. Zooming in on Figure 4c, the developed memristive devices with Cs_2CO_3 offer resistance states with extremely low energy consumption, down to ≈0.025 fJ bit^{-1} per cell (Figure 4d), achieving one of the lowest values ever reported compared to previous CAM technologies (see Table S5, Supporting Information). However, the energy consumption of the reference nCAM using the control perovskite devices goes up to 0.69 fJ bit^{-1} per cell (Figure S24, Supporting Information). A major reason for large differences between the energy consumption in different states is the amount of current flow at the different resistance states. The high resistance Cs_2CO_3-deposited perovskite memristor shows favorable parameters for the nCAM architecture to perform line-rate operations with minimum energy consumption in neuromorphic computing systems.

Finally, it is important to discuss the feasibility of miniaturizing these devices for dense integration with standard CMOS electronics, as required for the nCAM architecture. A recent report describes a 7 × 7 crossbar array utilizing Pb-based low-dimensional halide perovskites with a feature size of 100 µm.[38] However, due to their soft nature, metal halide perovskites are incompatible with standard lithography techniques. Nevertheless, alternative approaches, such as a combination of printing and laser etching, can enable feature sizes below 100 µm.[39] Furthermore, alternative device geometries that do not rely on lithography could be explored.[8,40]

3. Conclusion

We have developed a robust 2D layered RP Pb—Sn halide system with the addition of Cs_2CO_3 for high-performance and energy-efficient memristive devices. When employing Au top electrodes, excellent endurance (5×10^5 cycles), ON/OFF ratio (≈10^5), storage stability (5 months), and synaptic behaviors (STDP etc.) are displayed. The excellent synaptic properties are explained by photoluminescence spectroscopy and temperature-dependent impedance spectroscopy, which reveal the controlled introduction of trap states with the Cs_2CO_3 deposition. With the obtained memristive parameters, a remarkable accuracy (90.1%) in handwritten digit MNIST recognition is achieved. Furthermore, based on the developed perovskite memristive devices, an analog nCAM architecture is proposed for performing line-rate operations with ultralow energy consumption (≈0.025 fJ bit^{-1} per cell) in neuromorphic computing. Our results provide a prime example of the potentiality of low-dimensional metal halide materials for memristive devices.

Supporting Information

Supporting Information is available from the Wiley Online Library or from the author.

Acknowledgements

The authors are thankful for the technical support of Lai-Hung Lai, Arjen Kamp, and Teo Zaharia. The authors would like to acknowledge the financial support of the CogniGron research center and the Ubbo Emmius Funds (Univ. of Groningen). L.C. acknowledges the China Scholarship Council. J.L. and M.A.L. would like to acknowledge the financial support of the European Union (ERC-AdvancedGrant, DEOM, 101 055 097). F.T. thanks the Italian Ministry of Research (MUR) for co-financing a PhD position under the PON "Ricerca e Innovazione" 2014–2020 program FSE REACT-EU, decree 1061/2021.

Conflict of Interest

The authors declare no conflict of interest.

Author Contributions

L.C. fabricated the memristive devices and performed all the experiments. S.S. and B.K. designed the circuits and analyzed the perovskite-based nCAM. F.T. and N.M. conducted the GIWAXS measurements and analysis. J.L. assisted with the impedance spectroscopy analysis. L.D.M. measured the photoluminescence spectra. Z.X. and C.J.B. contributed to the neuromorphic computing and discussions. L.C. and M.A.L. conceived the idea and designed the experiments. M.A.L. supervised the whole project. All authors wrote the paper and participated in discussions.

Data Availability Statement

The data that support the findings of this study are available from the corresponding author upon reasonable request.

Keywords

2D layered Pb—Sn perovskite, analog CAM, neuromorphic computing, trap states

Received: September 24, 2024
Revised: March 2, 2025
Published online: March 31, 2025

[1] S. Kumar, X. Wang, J. P. Strachan, Y. Yang, W. D. Lu, *Nat. Rev. Mater.* **2022**, *7*, 575.
[2] F. Aguirre, A. Sebastian, M. L. Gallo, W. Song, T. Wang, J. J. Yang, W. Lu, M. F. Chang, D. Ielmini, Y. Yang, A. Mehonic, A. Kenyon, M. A. Villena, J. B. Roldan, Y. Wu, H. H. Hsu, N. Raghavan, J. Sune, E. Miranda, A. Eltawil, G. Setti, K. Smagulova, K. N. Salama, O. Krestinskaya, X. Yan, K. W. Ang, S. Jain, S. Li, O. Alharbi, S. Pazos, et al., *Nat. Commun.* **2024**, *15*, 1974.
[3] Z. Wang, S. Joshi, S. E. Savel'ev, H. Jiang, R. Midya, P. Lin, M. Hu, N. Ge, J. P. Strachan, Z. Li, Q. Wu, M. Barnell, G. L. Li, H. L. Xin, R. S. Williams, Q. Xia, J. J. Yang, *Nat. Mater.* **2017**, *16*, 101.
[4] Z. Xiao, Y. Yuan, Y. Shao, Q. Wang, Q. Dong, C. Bi, P. Sharma, A. Gruverman, J. Huang, *Nat. Mater.* **2015**, *14*, 193.

[5] E. J. Yoo, M. Lyu, J.-H. Yun, C. J. Kang, Y. J. Choi, L. Wang, *Adv. Mater.* **2015**, *27*, 6170.
[6] M. Vasilopoulou, A. R. b. Mohd Yusoff, Y. Chai, M.-A. Kourtis, T. Matsushima, N. Gasparini, R. Du, F. Gao, M. K. Nazeeruddin, T. D. Anthopoulos, Y.-Y. Noh, *Nat. Electron.* **2023**, *6*, 949.
[7] R. A. John, A. Milozzi, S. Tsarev, R. Brönnimann, S. C. Boehme, E. Wu, I. Shorubalko, M. V. Kovalenko, D. Ielmini, *Sci. Adv.* **2022**, *8*, ade0072.
[8] Y. Zhang, S. Poddar, H. Huang, L. Gu, Q. Zhang, Y. Zhou, S. Yan, S. Zhang, Z. Song, B. Huang, G. Shen, Z. Fan, *Sci. Adv.* **2021**, *7*, abg3788.
[9] C. Gu, J.-S. Lee, *ACS Nano* **2016**, *10*, 5413.
[10] Z. Xie, D. Zhang, L. Cheng, C. Li, J. Elia, J. Wu, J. Tian, L. Chen, M. A. Loi, A. Osvet, C. J. Brabec, *ACS Energy Lett.* **2024**, *9*, 948.
[11] R. A. John, Y. Demirag, Y. Shynkarenko, Y. Berezovska, N. Ohannessian, M. Payvand, P. Zeng, M. I. Bodnarchuk, F. Krumeich, G. Kara, I. Shorubalko, M. V. Nair, G. A. Cooke, T. Lippert, G. Indiveri, M. V. Kovalenko, *Nat. Commun.* **2022**, *13*, 2074.
[12] S. J. Kim, T. H. Lee, J.-M. Yang, J. W. Yang, Y. J. Lee, M.-J. Choi, S. A. Lee, J. M. Suh, K. J. Kwak, J. H. Baek, I. H. Im, D. E. Lee, J. Y. Kim, J. Kim, J. S. Han, S. Y. Kim, D. Lee, N.-G. Park, H. W. Jang, *Mater. Today* **2021**, *52*, 19.
[13] X. Zhu, Q. Wang, W. D. Lu, *Nat. Commun.* **2020**, *11*, 2439.
[14] Y. Ren, X. Bu, M. Wang, Y. Gong, J. Wang, Y. Yang, G. Li, M. Zhang, Y. Zhou, S. T. Han, *Nat. Commun.* **2022**, *13*, 5585.
[15] J. Yang, F. Zhang, H. M. Xiao, Z. P. Wang, P. Xie, Z. Feng, J. Wang, J. Mao, Y. Zhou, S. T. Han, *ACS Nano* **2022**, *16*, 21324.
[16] Y. R. Park, G. Wang, *Adv. Funct. Mater.* **2023**, *34*, 2307971.
[17] R. A. John, N. Shah, S. K. Vishwanath, S. E. Ng, B. Febriansyah, M. Jagadeeswararao, C. H. Chang, A. Basu, N. Mathews, *Nat. Commun.* **2021**, *12*, 3681.
[18] F. Zhou, Y. Liu, X. Shen, M. Wang, F. Yuan, Y. Chai, *Adv. Funct. Mater.* **2018**, *28*, 1800080.
[19] I. H. Im, J. H. Baek, S. J. Kim, J. Kim, S. H. Park, J. Y. Kim, J. J. Yang, H. W. Jang, *Adv. Mater.* **2024**, *36*, 2307334.
[20] Y. van de Burgt, E. Lubberman, E. J. Fuller, S. T. Keene, G. C. Faria, S. Agarwal, M. J. Marinella, A. Alec Talin, A. Salleo, *Nat. Mater.* **2017**, *16*, 414.
[21] M. M. Ganaie, G. Bravetti, S. Sahu, M. Kumar, J. V. Milic, *Mater. Adv.* **2024**, *5*, 1880.
[22] W. H. Qian, X. F. Cheng, Y. Y. Zhao, J. Zhou, J. H. He, H. Li, Q. F. Xu, N. J. Li, D. Y. Chen, J. M. Lu, *Adv. Mater.* **2019**, *31*, 1806424.
[23] L. Chen, J. Xi, E. K. Tekelenburg, K. Tran, G. Portale, C. J. Brabec, M. A. Loi, *Small Methods* **2024**, *8*, 2300040.
[24] F. Zeng, Y. Guo, W. Hu, Y. Tan, X. Zhang, J. Feng, X. Tang, *ACS Appl. Mater. Interfaces* **2020**, *12*, 23094.
[25] S. Y. Kim, J. M. Yang, E. S. Choi, N. G. Park, *Adv. Funct. Mater.* **2020**, *30*, 2002653.
[26] S. G. Kim, Q. Van Le, J. S. Han, H. Kim, M. J. Choi, S. A. Lee, T. L. Kim, S. B. Kim, S. Y. Kim, H. W. Jang, *Adv. Funct. Mater.* **2019**, *29*, 1906686.
[27] B. Hwang, J.-S. Lee, *Nanoscale* **2018**, *10*, 8578.
[28] J.-Y. Mao, Z. Zheng, Z.-Y. Xiong, P. Huang, G.-L. Ding, R. Wang, Z.-P. Wang, J.-Q. Yang, Y. Zhou, T. Zhai, S.-T. Han, *Nano Energy* **2020**, *71*, 104616.
[29] G. Pedretti, C. E. Graves, S. Serebryakov, R. Mao, X. Sheng, M. Foltin, C. Li, J. P. Strachan, *Nat. Commun.* **2021**, *12*, 5806.
[30] S. Saleh, B. Koldehofe, *Pro. of the 18th ACM Int. Symp. on Nanoscale Architectures*, Dresden, Germany, December, **2023**, p. 1.
[31] C. Li, C. E. Graves, X. Sheng, D. Miller, M. Foltin, G. Pedretti, J. P. Strachan, *Nat. Commun.* **2020**, *11*, 1638.
[32] D. Cortecchia, S. Neutzner, A. R. Srimath Kandada, E. Mosconi, D. Meggiolaro, F. De Angelis, C. Soci, A. Petrozza, *J. Am. Chem. Soc.* **2017**, *139*, 39.
[33] R. A. Awni, Z. Song, C. Chen, C. Li, C. Wang, M. A. Razooqi, L. Chen, X. Wang, R. J. Ellingson, J. V. Li, Y. Yan, *Joule* **2020**, *4*, 644.
[34] C. Gonzales, A. Guerrero, J. Bisquert, *Appl. Phy. Lett.* **2021**, *118*, 7.
[35] Y. Shao, Z. Xiao, C. Bi, Y. Yuan, J. Huang, *Nat. Commun.* **2014**, *5*, 5784.
[36] H. H. Fang, E. K. Tekelenburg, H. Xue, S. Kahmann, L. Chen, S. Adjokatse, G. Brocks, S. Tao, M. A. Loi, *Adv. Opt. Mater.* **2022**, *11*, 2202038.
[37] S. Saleh, B. Koldehofe, *IEEE Access* **2022**, *10*, 129279.
[38] S. J. Kim, I. H. Im, J. H. Baek, S. Choi, S. H. Park, D. E. Lee, J. Y. Kim, S. Y. Kim, N. G. Park, D. Lee, J. J. Yang, H. W. Jang, *Nat. Nanotechnol.* **2025**, *20*, 83.
[39] J. Semple, D. G. Georgiadou, G. Wyatt-Moon, M. Yoon, A. Seitkhan, E. Yengel, S. Rossbauer, F. Bottacchi, M. A. McLachlan, D. D. C. Bradley, T. D. Anthopoulos, *npj Flexible Electron.* **2018**, *2*, 18.
[40] J. J. de Boer, B. Ehrler, *ACS Energy Lett.* **2024**, *9*, 5787.